To cite this article：DU Z F, MU X L, LI Z J. Numerical analysis of influence of stern flaps on motion and stability of high-speed amphibious platform[J/OL]. Chinese Journal of Ship Research, 2022, 17(3). http://www.ship-research.com/en/article/doi/10.19693/j.issn.1673-3185.02331.

DOI：10.19693/j.issn.1673-3185. 02331

Numerical analysis of influence of stern flaps on motion and stability of high-speed amphibious platform

DU Zunfeng[*1], *MU Xuliang*[1], *LI Zhijun*[2]

1 State Key Laboratory of Hydraulic Engineering Simulation and Safety, School of Civil Engineering, Tianjin University, Tianjin 300354, China

2 Tieying Special Vehicles Co., Ltd., Tianjin 300232, China

Abstract: [**Objectives**] Stern flaps have a significant impact on the water performance of high-speed amphibious platforms. This paper discusses the influence of stern flaps on the motion and hydrodynamic characteristics of a high-speed amphibious platform in a sliding state. [**Method**] Using the SST k-ω turbulence model and overset grid technology, the CFD numerical simulations of an amphibious platform's high-speed navigation under static water conditions are performed, and the motion response and stability of the platform with different stern flaps are analyzed. Considering the influence of the velocity, center of gravity, and angle of the stern flaps on the longitudinal motion of the platform, support vector machines (SVMs) are adopted to classify and recognize the boundary of its motion stability. [**Results**] The results show that the stern flaps reduce the sailing trim angle by changing the pressure distribution on the underside of the platform, and the larger the rotation angle of the stern flaps, the more significant the influence on motion stability; when the position of the center of gravity is the same, the maximum speed of the platform in a stable state is increased. [**Conclusion**] The application of stern flaps and the improvement of motion stability are of great significance for the development of high-speed amphibious platforms.

Key words: high-speed amphibious platform; stability of motion; hydrodynamic characteristics; stern flaps

CLC number：U661.2+2；U674.78

0 Introduction

As an efficient means of land and water transportation, an amphibious platform can undertake multiple tasks such as field reconnaissance, material transportation, water patrol, and beach landing, which is developing toward high-speed and super high-speed in terms of performance [1]. For better water performance of amphibious platforms, Yu et al. [2-4] optimized the outline from the perspective of factors including the sliding way angle and wheel lifting and factored in the influence of navigation environment on platform performance. This effort provides a reliable basis for the improvement in performance under various navigation conditions. However, most of the objects are medium- and low-speed displacement platforms, with no regard given to high-speed platforms. Ling et al. [5-6] studied the motion of high-speed planing craft. According to the results, the craft would see the "porpoising" effect at high speed, and its heave, trim angle, and response frequency would also increase with the rise in navigational velocity, which means a significant impact on the navigation stability. Compared with

Received：2021－03－25 **Accepted**：2021－05－31

Authors：DU Zunfeng, male, born in 1984, Ph.D., associate professor. Research interest: intelligent design of high-tech ships. E-mail: dzf@tju.edu.cn

MU Xuliang, male, born in 1998, master degree candidate. Research interests: hydrodynamic performance of amphibious platforms and computational fluid dynamics. E-mail: 18202614551@163.com

LI Zhijun, male, born in 1987, engineer. Research interest: design and manufacture of amphibious vehicles. E-mail: junzhili@163.com

***Corresponding author**：DU Zunfeng

high-speed craft, an amphibious platform reports a smaller length-breadth ratio. In addition to the research on shape-based drag reduction, its navigation attitude and stability at high speed cannot be ignored still more.

As a common efficiency increase device for planing craft and other high-performance ships, appendage devices such as stern flaps and interceptors can reduce the pitch and heave amplitude, which shows that appropriate installation can improve the navigation attitude of ships [7-9]. Meanwhile, relevant studies have also suggested that wing plate-assisted devices can significantly improve the navigation performance and attitude of amphibious platforms at medium- and low-speed stages [10]. As the research on stern flaps rarely involves high-speed amphibious platforms, it is necessary to analyze the hydrodynamic characteristics of amphibious platforms during high-speed navigation in combination with stern flaps.

In recent years, the development of computational fluid dynamics (CFD) numerical simulation has provided good technical support for research on the performance of ships and water platforms [11-12]. Taking an amphibious platform as the research object, this paper will deal with the influence of stern flaps on it during high-speed navigation. First, we adopt the numerical method of CFD for simulations and computation of the platform under high-speed navigation, analyze the hydrodynamic action mechanism of the stern flaps, and then study the characteristics of their influence on the longitudinal motion attitude of the platform, i.e., influencing characteristics of dynamic response. On the basis of the computed results and the classification method of the support vector machine (SVM), we attempt to identify the motion stability boundary of the platform under different working conditions, so as to provide a reference for the performance improvement in the high-speed amphibious platform.

1 Numerical method and verification

1.1 Numerical computation method

In the Cartesian coordinate system, the governing equations of continuity and momentum conservation for the incompressible fluid flowing around the platform are presented as follows:

$$\frac{\partial \rho}{\partial t}+\frac{\partial(\rho u_i)}{\partial x_i}=0 \tag{1}$$

$$-\frac{\partial P}{\partial x_i}+\frac{\partial}{\partial x_j}\left(\mu\frac{\partial u_i}{\partial x_j}-\rho\overline{u_i' u_j'}\right)+S_i \tag{2}$$

where u_i and u_j are the time average velocity components in the direction of x_i and x_j, respectively, and $i, j = 1, 2, 3$; u_i' and u_j' are the fluctuation velocity components in the two directions, respectively; ρ stands for the fluid density of the object; t is time; P is the time average pressure of fluid; μ is the dynamic viscosity coefficient; $\rho\overline{u_i' u_j'}$ is the Reynolds stress term; S_i is the generalized source term of the momentum equation.

We adopt the finite volume method (FVM) to discretize the governing equations of flow, with the non-intersecting control units formed through grid division and the mass and momentum conservation of the whole field decomposed into finite integrals on each control unit [13]. The convection term adopts the quadratic upstream interpolation for convective kinetics (QUICK) scheme, and the discretization of the diffusion term uses the central difference scheme, with the SIMPLE separation algorithm for solutions.

We introduce the two-equation turbulence model, the shear stress transfer (SST) k-ε model, to make the governing equations closed and solvable. This model uses a mixed function, with the k-ω and k-ε models adopted within and outside the boundary layer, respectively, and the governing equations contain the cross-diffusion term away from the wall.

We use the volume of fluid (VOF) method based on Euler multiphase flow to capture the free surface. In other words, when a unit is filled with liquid-phase fluid, its volume fraction C_{q}=1, and when a unit is filled with gas-phase fluid, C_{q}=0, with the approximate position of the free surface determined by the calculation of the volume fraction of liquid-phase fluid in each unit [14]. Its continuity equation is expressed by

$$\frac{\partial C_{\mathrm{q}}}{\partial t}+u_i\frac{\partial C_{\mathrm{q}}}{\partial x_i}=0 \tag{3}$$

We divide the computational domain into the background domain and overset domain, where the former remains static, and the latter reports the motion of the ship. The separate generation of the grids in the two domains helps avoid the deformation of the grids in the whole computational domain with the motion of the ship. We keep the grid dimension at the junction of the two domains at the same level to reduce the numerical error and carry out the information transmission between the two sets of grids through linear interpolation. The longitudinal motion of the hull involves two degrees of freedom (2DOF), including pitch and heave. According to the center-of-mass motion and the theorem of the moment of momentum around the center of mass, its motion equations are written as

$$F_z = m\frac{\mathrm{d}^2 Z_g}{\mathrm{d}t^2} \tag{4}$$

$$M_y = I_y\frac{\mathrm{d}^2\theta}{\mathrm{d}t^2} \tag{5}$$

where F_z and M_y are the vertical force and longitudinal moment acting on the hull, respectively, which are solved via integration; m is the mass of the amphibious platform; Z_g is the vertical displacement of the center of gravity of the hull; θ is the pitch angle of the hull; I_y is the moment of inertia of the hull around the longitudinal axis.

1.2 Numerical computation verification

To ensure the reliability of numerical computation, we verify the numerical computation method with the test results of the generic prismatic planning hull (GPPH) and compare the computed results with the data in the test and References [15-16]. Fig. 1 shows the outline of GPPH, and Table 1 lists the principal dimensions and relevant parameters of the craft.

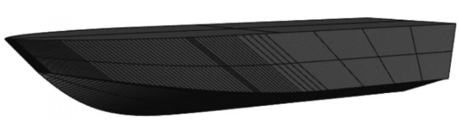

Fig. 1 Outline of GPPH planing craft

Table 1 Parameters of GPPH planing craft

Paramter	Value
Craft length L_1 /m	2.410
Craft breadth B_1 /m	0.630
Mass m_1 /kg	101.250
Distance between center of gravity and stern x_1 /m	0.844
Height from center of gravity to baseline z_1 /m	0.138
Longitudinal moment of inertia I_{yy} /(kg·m^2)	20.940
Draft under static floating D_1 /m	0.148

The grid division structure of the overset domain and the background domain is shown in Fig. 2, in which the size of the former is $5L_1 \times 2L_1 \times 2L_1$, and that of the latter is $1.5L_1 \times 0.4L_1 \times 0.4L_1$. We appropriately encrypt the peripheral area of the overset grids to ensure a scientific transition between the grids in the two domains while refining accordingly the grids of the waterline surface and the Kelvin wave area at the stern. According to the computation experience of ship CFD, we set the grid size of the hull surface as 8 ‰ of the craft length, the y+ value of the wall as 50, the number of boundary layers on the surface as 6, and the growth rate as 1.3.

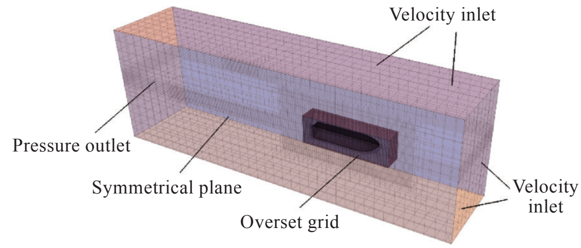

Fig. 2 Grid and boundary setting

According to the position and direction of the incoming flow, the upper, lower, and front boundaries of the hull are set as velocity inlets, and the boundary pressure at the stern is set as the outlet boundary. The left and right boundaries are taken as the symmetrical planes according to the symmetry of motion calculation, with VOF wave damping applied in the pressure outlet area to weaken the backflow effect due to numerical reflection at the outlet.

Given the results of the numerical computation of GPPH presented in Fig. 3, it is found that the results of the trim angle and wetted length of the keel line share the same variation characteristics as those in the test and Reference [16], and the error is relatively small. In other words, the numerical simulation of the ship under high-speed navigation by the above numerical computation method can lead to more accurate motion response results.

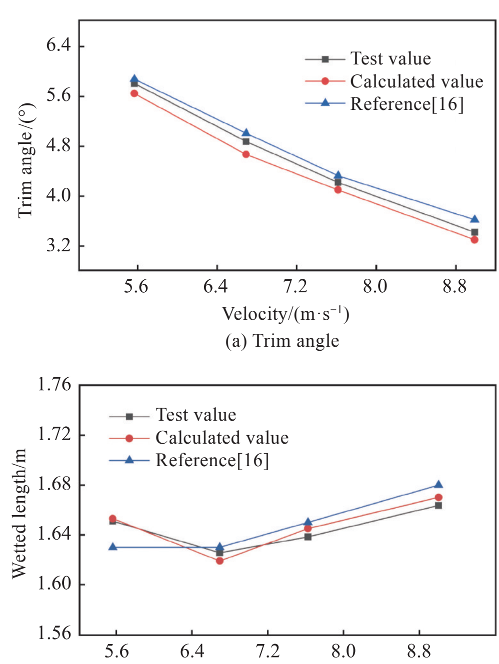

(a) Trim angle

(b) Wetted length

Fig. 3 Verification results of the numerical method

2 Analysis of high-speed motion of the amphibious platform

The high-speed planing amphibious platform, the research object of this study, has a volume Froude number of $Fr_V \approx 3.0$ at a high speed of v=20−25 kn. As the navigation state is similar to that of high-speed craft, we continue to use the above numerical method adopted for GPPH to carry out the numerical computation of the real-scale platform in high-speed motion, with the size of the computational domain and the grid dimension determined on the basis of the total length L of the amphibious platform. Table 2 presents the information on the principal dimensions of the platform, and Fig. 4 demonstrates the outline of the platform and the structural diagram of the stern flaps, in which the stern flaps are distributed on both sides of the longitudinal section in the center plane of the platform, with its rotation angle represented by α (unit: (°)).

Table 2 Parameters of the amphibious platform

Paramter	Value
Total length L/m	6.00
Waterline length L_{WL}/m	5.69
Molded breadth B/m	2.36
Draft D/m	0.42
Displacement Δ/t	3.20
Height from center of gravity to bottom plate z_g /m	0.30
Stern flap length /m	0.15
Stern flap breadth /m	0.34

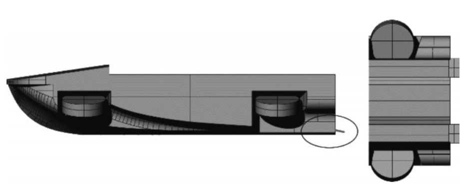

Fig. 4 Outline of the amphibious platform and stern flaps

With the above numerical method, we analyze the surface grid sensitivity of the amphibious platform. In the calculation, the platform surface will be divided into fine, medium, and coarse grids of 14, 20, and 28 mm, the dimensions of which are 0.23%, 0.33%, and 0.46% of the total length of the platform, respectively. By the grid refinement method in the computational domain, the number of grids for the three schemes is 1.15×10^7, 5.03×10^6, and 2.33×10^6, respectively.

As this study focuses on the analysis of the influence of the stern flaps on the longitudinal motion of the amphibious platform, we select the stern flaps with an angle of α = 8° and 23° for verification, with a verification speed of 22 kn. Table 3 presents the results of the navigation attitude of the platform calculated in the presence of the three types of grids separately. It is indicated that the difference between the results of the trim angle and the heave is small at different grid levels, and the difference between the platform attitudes decreases with the gradual refinement of the grid dimension, showing a trend of convergence. Upon overall consideration of the calculation efficiency and accuracy, we confirm that the size of the grids on the platform surface is 20 mm, and the refined size of the grids on the stern flap surface is 5 mm. As the flow field is symmetrical about the longitudinal section in the center plane of the platform, the numerical computation with a half-side flow field is performed, with the grid division at the stern flaps shown in Fig. 5.

Table 3 Results of grid sensitivity

Size of surface grid/mm	α=8°		α=23°	
	Trim angle/(°)	Heave/m	Trim angle/(°)	Heave/m
14	4.36	0.318	1.66	0.254
20	4.23	0.316	1.55	0.256
28	3.89	0.319	1.54	0.256

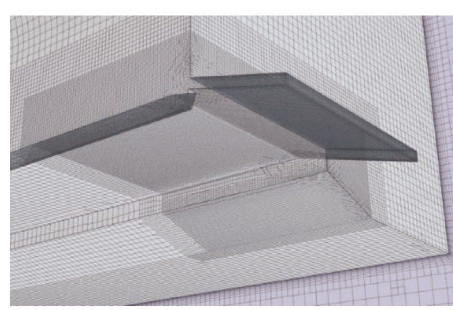

Fig. 5 Grid division of stern flap

2.1 Hydrodynamic performance analysis of stern flaps

2.1.1 Influence on longitudinal motion

To make a qualitative analysis of the influence of stern flaps on the hydrodynamic performance of a high-speed amphibious platform, we calculate the motion characteristics of the platform under the action of stern flaps at different rotation angles. Table 4 shows the corresponding results of the trim angle and relative heave at v = 22 kn, with the center of gravity 0.43L from the stern plate in the longitudinal direction.

According to Table 4, the trim angle of the plat-

Table 4 Results of longitudinal motion at a speed of 22 kn

α/(°)	Trim angle/(°)	Heave /m
No stern flap	4.61	0.34
2	4.50	0.33
8	4.23	0.31
15	2.95	0.28
23	1.55	0.26

form decreases with the increase in the rotation angle α of the stern flaps—a larger α is accompanied by a more significant reduction in the trim angle. In the meanwhile, the overall heave of the platform also declines as α rises. This may be explained by the fact that as the stern flaps acts on the stern, this has a relatively significant influence on the trim angle but has no remarkable vertical lifting effect on the whole platform; on the contrary, the heave also decreases due to the reduction in the trim angle.

2.1.2 Influence on wave-current field and pressure field

To study the influence of stern flaps on the waveform in the wake field of the platform, we analyze the waveforms at different longitudinal sections under different α. With the distances from the selected longitudinal sections to the longitudinal sections in the center plane being Y = 0, 0.55, 1.0, and 1.75 m, the stern flaps are placed at the stern of the platform, 0.55 m away from the longitudinal section in the center plane. Fig. 6 presents the waveform results at each section, where X stands for the coordinate of the longitudinal position.

It is indicated from Fig. 6 that the stern flaps have an insignificant influence on the far-field waveform. Under the action of the stern flaps at different rotation angles, the far-field waveform is generally the same, with the main range of action close to the stern flaps, a radius of about 6−12 m. With the increase in α, the waveform at Y = 0.55 m decreases significantly behind the stern flaps, with its "false tail" length largely the same; while on both sides of the stern flaps, the waveforms at the positions of Y = 0 m and Y = 1.0 m rise significantly due to the extrusion of the stern flaps. Outside the breadth of the platform, i.e., at the position of Y = 1.75 m, the peak elevation and trough depth decrease with the increase in α, which suggests some effect of the stern flaps on the improvement of the wave-current field at a high speed.

The stern flaps do not only influence the wave-current field but also act on the pressure distribution at the bottom of the platform more significantly to result in the induced lift. Fig. 7 shows the comparison of pressure distributions at the bottom of the platform under different α. It is indicated that the presence of the stern flaps leads to an obvious area of relatively high pressure at the platform stern, which mainly acts on the breadth range of the stern flaps, and a larger α leads to a more prominent high-pressure area. We intercept the buttock line of the underside at Y = 0.55 m in the rear half of the plat-

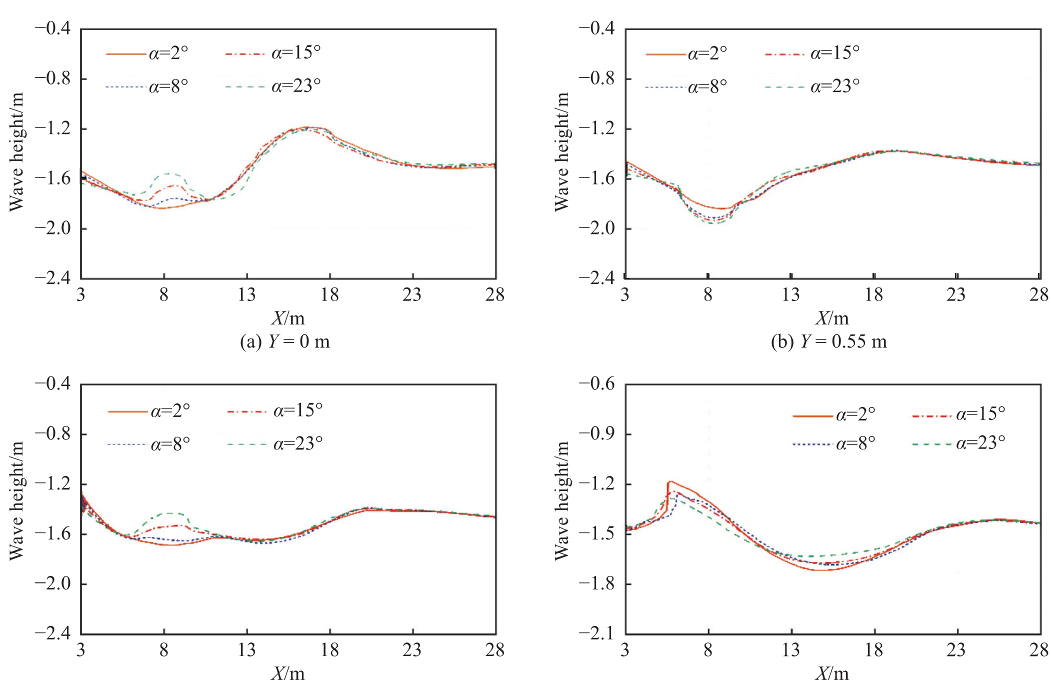

Fig. 6 Comparison of wave height at different longitudinal sections

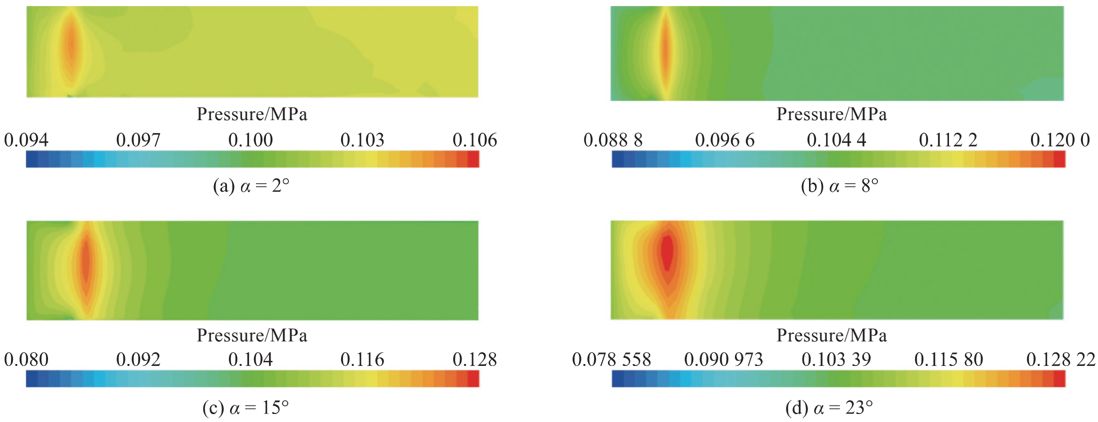

Fig. 7 Relative pressure distribution at the bottom of the platform under different α

form and compare the relative pressure on the stern flaps and the bottom of the platform at different α when v = 22 kn, as shown in Fig. 8. Insignificant when α is close to 0°, the pressure peak formed on the stern flaps rises remarkably when α = 8° and above, a relative increase of more than 20%, and the longitudinal influence also keeps expanding.

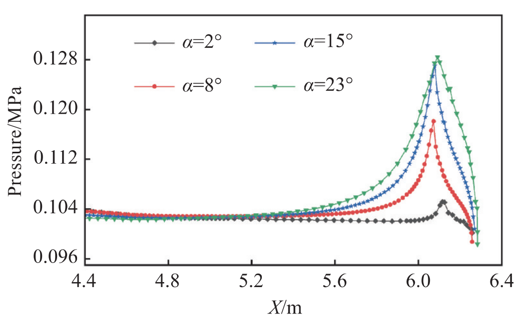

Fig. 8 Relative pressure on longitudinal section of stern flaps and platform under different α (v = 22 kn)

According to the above analysis, the stern flaps generate noticeable induced lift at the stern by affecting the pressure distribution at the bottom to form a longitudinal plough-in moment, whose influence on the longitudinal motion of the platform is presented as the reduction in the trim angle and heave. It follows that with external disturbance, a smaller motion response of the platform makes it easier to maintain stability, and in this way, the motion stability of the platform can be improved.

2.2 Analysis of longitudinal motion stability

2.2.1 Design parameters and their influence on stability

We define the ratio of the longitudinal distance from the center of gravity to the stern plate to the total length L of the platform as r. At the same position of the center of gravity, a higher speed means worse motion stability, while at the same speed, a farther position of the center of gravity is more likely to cause instability of the longitudinal motion. As shown in Fig. 9, when the center of gravity and the state of the stern flaps remain unchanged, with the rise in speed, the amplitude of the trim angle also increases, and the convergence slows down.

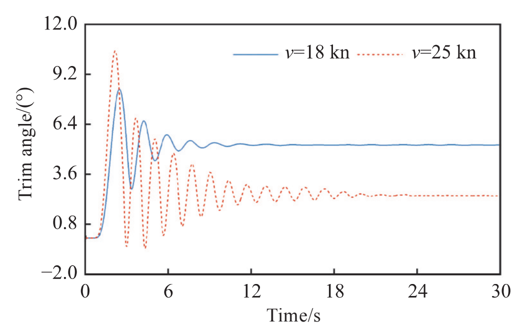

Fig. 9 Attitude convergence at different speed (α = 15°, r = 0.40)

With the ratio r, the speed v of the platform, and the rotation angle α of the stern flaps as the design variables, the value range of r being [0.35, 0.50], and that of v being [10, 28], we select multiple sample points randomly in the design space composed of the longitudinal position of the center of gravity r and the speed v, with α = 2°, 8°, 15°, and 23°. Then, we carry out numerical computation of these points and count the numerical characteristics of the longitudinal motion stability corresponding to each point.

In the case of v = 22 kn and r = 0.43, the convergence curves of the trim angle in different states of stern flaps in Fig. 10 show that the presence of the stern flaps also reduces the fluctuation of the platform pitch and makes its pitch attitude converge to a generally stable value. On the contrary, the case where the stern flaps are not installed reports significant amplitude of the motion attitude, which means

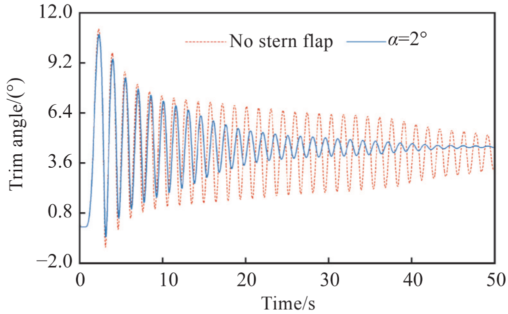

Fig. 10 Attitude convergence in different states of stern flaps (v = 22 kn, r = 0.43)

the stability cannot be ensured.

2.2.2 Motion stability classification based on SVM

The data classification based on SVM works mainly by determining an N-dimensional optimal classification hyperplane to maximize the interval between the sample data points closest to the plane on both sides of the hyperplane while dividing two types of data with different numerical characteristics to both sides of the hyperplane. Then, it uses the hyperplane as the distribution boundary between the two types of data [17]. When $N = 2$, the hyperplane is a two-dimensional straight line; for $N \geqslant 2$, the general form of hyperplane is $\boldsymbol{\omega}^{\mathrm{T}}\boldsymbol{x} + b = 0$, where $\boldsymbol{x}$ stands for the data point; $\boldsymbol{\omega}$ is the normal vector of the plane, and b denotes the plane intercept. The objective function of the maximal interval optimization problem of the hyperplane is presented as

$$\arg\max\left\{\min(y(\boldsymbol{\omega}^{\mathrm{T}}\boldsymbol{x}+b))\frac{1}{\|\boldsymbol{\omega}\|}\right\} \quad (6)$$

Assume the characteristic label y of different types of data points is 1 or −1, we can simplify the objective function of the optimization problem, i.e.,

$$\min \ \frac{1}{2}\|\boldsymbol{\omega}\|^2 \quad (7)$$

$$\text{s.t. } y(\boldsymbol{\omega}^{\mathrm{T}}\boldsymbol{x}+b)-1\geqslant 0 \quad (8)$$

Given Eqs. (7) and (8), we introduce the Lagrange multiplier parameter $\boldsymbol{\alpha}=[\alpha_1, \alpha_2,\cdots,\alpha_i,\cdots,\alpha_n]$, adjust the initial optimization for determining the optimal hyperplane to the optimization for solving the Lagrange parameter vector $\boldsymbol{\alpha}$, as shown in Eqs. (9) and (10). In the equations, $L(\boldsymbol{\alpha})$ stands for the simplified expression of the objective function; α_i and α_j are the Lagrange multiplier parameters corresponding to $\boldsymbol{x}_i$ and $\boldsymbol{x}_j$, and $k(\boldsymbol{x}_i, \boldsymbol{x}_j)$ is the kernel function. For the case of the linear inseparability of the sample data on a low-dimensional plane, we can make it linearly separable by introducing a non-linear kernel function and mapping it to a high-dimensional space. In this paper, we carry out the mapping transformation of the collected two-dimensional data points by use of the polynomial kernel function, with its general expression shown in Eq. (11), where a, c, and d represent manually specified constants.

$$\min\ L(\boldsymbol{\alpha})=\sum_{i=1}^{n}\alpha_i-0.5\sum_{i,j=1}^{n}\alpha_i\alpha_j y_i y_j\cdot k(\boldsymbol{x}_i,\boldsymbol{x}_j) \quad (9)$$

$$\text{s.t.}\ \sum\alpha_i y_i=0;\quad \alpha_i\geqslant 0,\quad i=1,2,\cdots,n \quad (10)$$

$$k(\boldsymbol{x}_i,\boldsymbol{x}_j)=(a\boldsymbol{x}_i{}^{\mathrm{T}}\boldsymbol{x}_j+c)^d \quad (11)$$

For each different rotation angle α of stern flaps, we classify the collected samples according to the stability characteristics obtained via CFD calculation and apply the SVM classification algorithm to identify the classification hyperplane between the stability and instability in longitudinal motion. As to the time-history curve of attitude calculated for different sample points, if it does not show an obvious trend of convergence in a certain period of time, the sample point is judged as an instability point. Since the stability characteristics of the points on the hyperplane cannot be identified in theory, we will use 28 s as the time standard when assigning the stability characteristics to the collected samples to ensure the reliability of stability state classification. In this way, we can make the classification hyperplane obtained more inclined to the stable side. Fig. 11 presents the classification results of the sample points at different α.

For the classification results shown in Fig. 11, given the possible inaccurate classification results due to partial dense or sparse distribution of sample points in the classification, we reduce the speed values of the steady-state points that are too close to or even cross the boundary in the figure, e. g., the steady-state points near r = 0.45 when α = 2° and those near r = 0.47 when α = 8°. Then, we add new sampling points in the area where the samples are sparsely distributed, e.g., the two sample points added at r = 0.47, v = 23 kn and r = 0.37, v = 20 kn when α = 23°. Afterward, we carry out CFD calculations for the adjusted and newly added sample points again and classify the data on the basis of the stability results. Fig. 12 shows the results after reclassification, in which the upper left area of each curve represents the motion instability area corresponding to α.

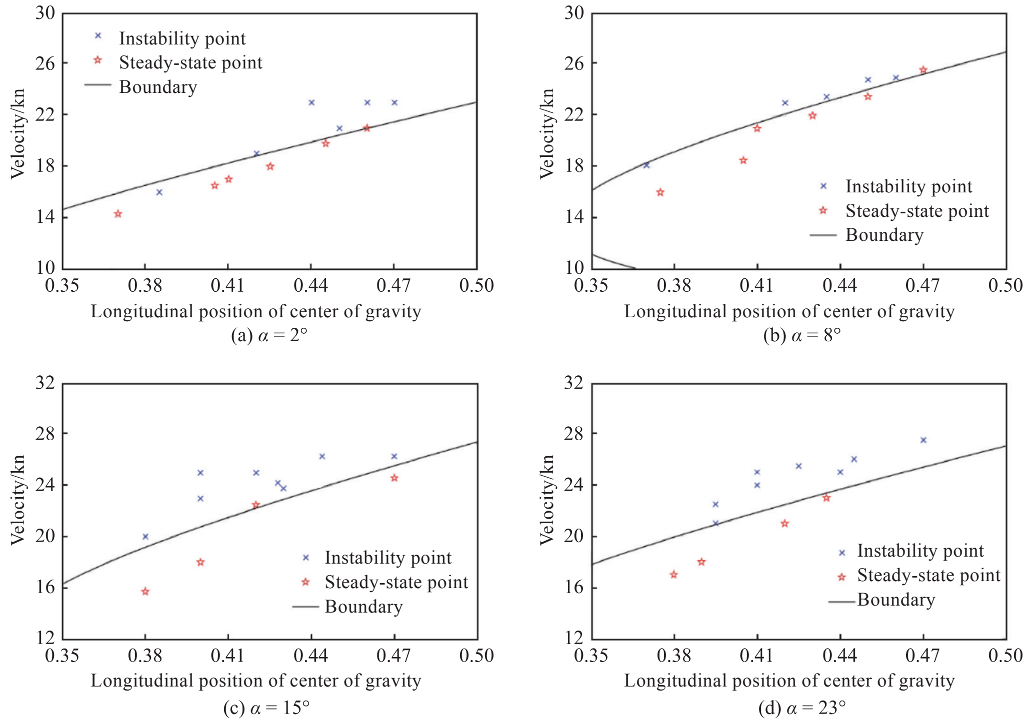

Fig. 11 Stability classification results at different α

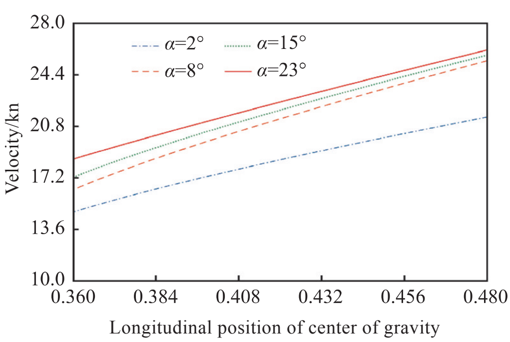

Fig. 12 Boundary of platform stability at different α

Finally, we obtain the numerical expressions of the boundary of platform motion stability through classification when α = 2°, 8°, 15°, and 23°, as shown in Eqs. (12)−(15) respectively. In these equations, r represents the longitudinal position of the center of gravity of the horizontal ordinate, i.e., the ratio of the longitudinal distance from the center of gravity to the stern plate to the total length L of the platform, and s denotes the speed of the amphibious platform, i.e., the vertical ordinate shown in Fig. 12.

$$0.064\,6r^2-0.080\,7s^2+2.867\,9rs+0.303\,6r+0.774\,4s=0 \tag{12}$$

$$0.059\,8r^2-0.062\,5s^2+3.189\,7rs+0.282\,4r+0.379\,3s=0 \tag{13}$$

$$0.058\,0r^2-0.064\,5s^2+3.031\,4rs+0.278\,5r+0.576\,5s=0 \tag{14}$$

$$0.037\,4r^2-0.039\,4s^2+1.967\,7rs+0.186\,8r+0.236\,2s=0 \tag{15}$$

According to the classification results of the longitudinal motion stability of the platform, when other parameter factors remain unchanged, it is possible to increase the upper speed limit that can be reached in the stable state by the adjustment to the longitudinal position of the center of gravity. The insignificant range of the change in the positions of the center of gravity of the platform, however, is not of great significance to the improvement in the steady speed, and thus we confirm that the steady speed that the amphibious platform can reach without other appendages does not exceed 21 kn.

Nevertheless, it is possible to significantly improve the stability of the longitudinal motion of the platform at different speeds by the installation of stern flaps with rotation angles at the stern. As shown in Fig. 12, when the rotation angle α increases from 2° to 8°, the platform reports a significant increase in the maximum speed that can be reached in a stable state, but as α continues to increase, this effect begins to weaken. In addition, the comparison and statistics of the effects of angle-variable stern flaps at different positions of the center of gravity reveal that when α = 23°, the maximum steady speed that the platform can reach increases by about 19% on average compared with the case when α = 2°. When the center of gravity is 0.46L from the stern plate, the maximum steady speed can reach 25 kn.

3 Conclusions

This paper studies the influence of stern flaps on the longitudinal motion and hydrodynamic performance of a high-speed amphibious platform. The following conclusions are drawn:

1) Stern flaps have little effect on the wavelength of the far field behind the platform. As the rotation angle of the stern flaps increases, the amplitude of hull-making wave near the "false tail" will rise, and the wave peak on both sides of the platform will also decrease as the trim angle declines accordingly.

2) Stern flaps can change the pressure field at the bottom of the amphibious platform, which leads to a concentrated high-pressure area at the stern. When the rotation angle α increases from 0° to about 23°, the high-pressure area grows significantly.

3) By changing the pressure field distribution at the bottom of the platform to induce the plough-in moment, stern flaps can reduce the fluctuation of its longitudinal motion and accelerate the convergence of attitude stability while reducing the running trim angle to improve the navigational stability of the amphibious platform.

4) By improving the longitudinal motion stability of the platform at different speed, we found that stern flaps can delay the boundary between motion stability and instability, and the presence of stern flaps at the same position of the center of gravity greatly advances the maximum steady speed of the platform.

References

[1] JU N J.Hydrodynamics analysis and simulation for amphibious vehicle [M]. Beijing: The Publishing House of Ordnance Industry, 2005: 386−421 (in Chinese).

[2] YU Z Y, LIAO Y C, LI J Y, et al.Simulation analysis of effect of different skateboard angles on lift-drag ratio of amphibious vehicle [J]. Ship Engineering, 2015, 37 (3): 26−29 (in Chinese).

[3] MAIMUN A, NAKISA M, TARMIZI A, et al. Numerical study on hydrodynamic resistance of new hull design for multipurpose amphibious vehicle [J]. Applied Mechanics and Materials, 2014, 663: 522−531.

[4] NAKISA M, MAIMUN A, AHMED Y M, et al. Numerical estimation of shallow water effect on multipurpose amphibious vehicle resistance [J]. Journal of Naval Architecture and Marine Engineering, 2017, 14 (1): 1−8.

[5] LING H J, WANG Z D. Real-time numerical prediction method of “Dolphin Motion” high-speed planning craft [J]. Journal of Shanghai Jiaotong University, 2014, 48 (1): 106−110 (in Chinese).

[6] MANSOORI M, FERNANDES A C. The interceptor hydrodynamic analysis for controlling the porpoising instability in high speed crafts [J]. Applied Ocean Research, 2016, 57: 40−51.

[7] SAKAKI A, GHASSEMI H, KEYVANI S. Evaluation of the hydrodynamic performance of planing boat with trim tab and interceptor and its optimization using genetic algorithm [J]. Journal of Marine Science and Application, 2019, 18 (2): 131−141.

[8] LI D Q, LI P, ZHANG Y L, et al. Influence of segmented stern flap on resistance performance of high speed craft [J]. Ship Engineering, 2019, 41 (7): 37−43 (in Chinese).

[9] SUN Y F, ZONG Z, JIANG Y C.Review of longitudinal motion and controls of ships on waves [J]. Chinese Journal of Ship Research, 2020, 15 (1): 1−12, 47 (in Chinese).

[10] LEE S J, LEE T I, LEE J J, et al. Hydrodynamic characteristics of a hydrofoil-assisted amphibious vehicle [J]. Journal of Ship Research, 2017, 61: 15−22.

[11] WANG S X, JIN G Q, WANG H, et al. Research on the hydrodynamic performance of a double-carriage amphibious vehicle sailing in still water [J]. Acta Armamentarii, 2020, 41 (3): 434−441 (in Chinese).

[12] JIA J B, ZONG Z, JIN G Q, et al. A numerical investigation of sinkage and trim effects on the resistance of trimaran hull form in calm water [J]. Chinese Journal of Ship Research, 2020, 15 (6): 106−114 (in Chinese).

[13] JAVANMARD E, YARI E, MEHR J A, et al. Hydrodynamic characteristic curves and behavior of flow around a surface-piercing propeller using computational fluid dynamics based on FVM [J]. Ocean Engineering, 2019, 192: 106445.

[14] VASHAHI F, DAFSARI R A, REZAEI S, et al. Assessment of steady VOF RANS turbulence models in rendering the internal flow structure of pressure swirl nozzles [J]. Fluid Dynamics Research, 2019, 51 (4): 045506.

[15] LEE E, WEIL C R, FULLERTON A. Experimental results for the calm water resistance of the generic prismatic planing hull (GPPH): NSWCCD-80-TR-2017/015 [R]. Naval Surface Warfare Center Carderock Division, 2017.

[16] LI J H, BONFIGLIO L, BRIZZOLARA S. Verification and validation study of openfoam on the generic prismatic planing hull form [C] //MARINE VIII: Proceedings of the VIII International Conference on Computational Methods in Marine Engineering. CIMNE, 2019: 428−440.

[17] WEI H X, CHEN J F, ZHU J, et al. A new zoning method of blasting vibration based on energy proportion and its SVM classification models [J]. Shock and Vibration, 2021, 2021: 6697682.

压浪板对高速两栖平台运动稳定性影响的数值分析

杜尊峰*1, 慕旭亮1, 李志军2

1 天津大学 建筑工程学院 水利工程仿真与安全国家重点实验室,天津 300354

2 铁鹰特种车(天津)有限公司,天津 300232

摘　要:［目的］压浪板对两栖平台的水上性能具有显著影响,需探讨滑行状态下压浪板对高速两栖平台航行姿态及运动稳定性的影响规律。［方法］采用SST k-ω 湍流模型以及重叠网格技术,对高速状态下两栖平台的静水直航进行CFD数值仿真计算,比较不同压浪板作用下平台姿态及稳定性的变化特性,并利用支持向量机(SVM)进行速度、重心位置等因素影响下平台运动稳定性边界的分类识别。［结果］结果显示,压浪板通过改变平台底面的压力分布,可减小航行纵倾角,并且压浪板的下旋角度越大,对姿态稳定性的影响越显著;在重心位置相同的情况下,可提高平台稳定状态下能够达到的最大航速。［结论］研究表明减摇附体的应用及运动稳定性的提高对两栖平台的高速化发展意义重大。

关键词: 高速两栖平台; 运动稳定性; 水动力特性; 艉压浪板